Mechanics of Materials xxx (2009) xxx–xxx

Contents lists available at ScienceDirect

Mechanics of Materials

journal homepage: www.elsevier.com/locate/mechmat

Spall strength of a zirconium-based bulk metallic glass under shock-induced compression-and-shear loading

Fuping Yuan [a], Vikas Prakash [a,*], John J. Lewandowski [b]

[a] Department of Mechanical and Aerospace Engineering, Case Western Reserve University, 10900 Euclid Avenue, Glennan 616 B, Cleveland, OH 44106-7222, USA
[b] Department of Materials Science and Engineering, Case Western Reserve University, Cleveland, OH 44106-7222, USA

ARTICLE INFO

Article history:
Received 5 July 2008
Received in revised form 27 December 2008
Available online xxxx

ABSTRACT

We present results of a series of plate-impact experiments conducted to understand spall threshold in a zirconium-based bulk metallic glass (BMG), $Zr_{41.25}Ti_{13.75}Ni_{10}Cu_{12.5}Be_{22.5}$, following normal shock-induced compression and combined compression-and-shear loading. The experiments were conducted using a 82.5 mm bore single-stage gas-gun. A multi-beam VALYN VISAR was used to measure the particle–velocity at the free-surface of the target plate. For the normal shock-compression experiments, the impact velocities were chosen to span the elastic to the elastic–plastic range of the BMG during impact; the spall strength was inferred, at different levels of shock-induced compression, from the measured particle–velocity history of the free-surface of the target plate. For the combined compression-and-shear experiments the shock-induced normal stress was kept constant at ~5 GPa (i.e. below the HEL for the BMG), while the projectile skew angle was varied from 6° to 24°. These skew angles are expected to result in a maximum shear strains of up to 3.18%. Under normal impact, at impact stress levels below the HEL, the spall strength of the BMG was found to decrease with increasing levels of the impact stress. However, at impact stress levels above the HEL the spall strength is observed to remain constant with increasing impact stress at ~2.3 GPa. In the case of the combined compression-and-shear loading, with increasing levels of shear strain (at a constant shock-compression level below the HEL), the spall strength of the BMG was found to initially decrease, increase dramatically in the shear strain range of 2–2.4%, and then fall again as the shear strain is increased from 2.4% to 3.18%.

1. Introduction

Bulk amorphous metals, also referred to as bulk metallic glasses (BMG), are alloys in which super-cooling of a liquid alloy produces a metastable phase, thus preventing formation of crystals and leading to a lack of long-range periodicity. Due to their randomly-ordered atomic structures, BMGs are known to exhibit unusual mechanical properties such as near theoretical strength, large elastic strains, high hardness, excellent wear and corrosion resistance, and increased fracture toughness when compared to other brittle, high compressive strength materials (Bruck et al., 1996; Lowhaphandu and Lewandowski, 1998).

The dynamic response of BMGs is of considerable interest to gain insight into the high-strain rate response of this class of materials, and for potential applications, e.g. kinetic energy penetrators (Johnson, 1999). The first well documented high-strain rate compression tests on a Zr-based BMG, $Zr_{41.25}Ti_{13.75}Cu_{10}Ni_{12.5}Be_{22.5}$, were performed by Bruck (1994) using a Split-Hopkinson Pressure Bar (SHPB). In the study, under dynamic compression the yield strength of the BMG was found to be about 1.8 GPa at a strain rate of 10^3/s, and was largely insensitive to the applied strain rate. Failure occurred at 45° to the loading axis, which was virtually identical to the angle found from quasi-static compression tests. For another Zr-based BMG, i.e.

* Corresponding author. Tel.: +1 2163686440; fax: +1 2163683007.
E-mail address: vikas.prakash@case.edu (V. Prakash).

0167-6636/$ - see front matter © 2009 Published by Elsevier Ltd.
doi:10.1016/j.mechmat.2009.01.025

$Zr_{41.25}Ti_{13.75}Ni_{10}Cu_{12.5}Be_{22.5}$, Lu (2002) reported the strength under dynamic and quasi-static loading conditions to be quite similar, with failure being characterized by predominantly inhomogeneous inelastic flow. In addition, infra-red imaging of the experiments revealed temperature increase of up to 500° K during dynamic failure. Moreover, in both $Zr_{57}Ti_5Cu_{20}Ni_8Al_{10}$ and $Zr_{41.25}Ti_{13.75}Ni_{10}Cu_{12.5}Be_{22.5}$ BMGs, strain-rate softening was reported by Hufnagel et al. (2002). Such behavior was also observed when zirconium was replaced by hafnium (Subhash et al., 2003). More recently, Sunny et al., 2006a,b; 2005a,b have investigated the high-strain rate behavior of $Zr_{41.25}Ti_{13.75}Ni_{10}Cu_{12.5}Be_{22.5}$ by utilizing the SHPB. In their study, in situ high speed video was used to examine the deformation and failure modes under uniaxial dynamic compression. The as-received fully amorphous BMG was observed to exhibit catastrophic failure with the formation of a dominant shear band, while the annealed BMG specimens were observed to fail by extensive fragmentation after the formation of an initial crack. Moreover, the as-cast amorphous BMG specimens exhibited a reduction in peak stress as the L/D ratio of the specimens was reduced, with failure occurring at the specimen-insert interface, which was indicative of stress concentrations due to the difference in the specimen and SHPB bar diameters. A tapered insert was developed to alleviate the effects of stress concentrations. In some experiments, strain gages were attached directly to the specimens to determine the stress–strain response. With the tapered inserts, the as-cast and annealed BMG specimens exhibited failure in the gage section with little reduction in peak stress as the L/D ratio was reduced.

Even though the deformation and failure mechanisms of BMGs under moderate dynamic loading conditions ($\sim 10^3$/s) have been investigated, only a few studies have addressed the high impact velocity shock response of BMGs. Bach et al. (1991) studied parameters for the shock wave consolidation of a metallic glass powder, such as the effects of the shock wave energy and shock wave duration. Conner et al. (2000) investigated the high-strain rate behavior of fiber-reinforced $Zr_{41.2}Ti_{13.8}Cu_{12.5}Ni_{10}Be_{22.5}$ composites, and demonstrated their excellent potential as armor penetrators. Zhuang et al. (2002) conducted plate-impact experiments to investigate the shock response of a Zr-based BMG, $Zr_{41.2}Ti_{13.8}Cu_{12.5}Ni_{10}Be_{22.5}$ (Vitreloy-1), and its particulate composite, $Zr_{56.3}Ti_{13.8}Ni_{5.6}Cu_{6.9}Be_{12.5}$ (*in-situ* dendritic β-phase reinforced Vitreloy (Hays et al., 2000), which are to be, respectively, referred to as Vit-1 and β-Vit hereafter. A concave downward curvature in the shock Hugoniot was obtained, suggesting a phase-change like transition during the shock-compression event. The spalling in Vit-1 was induced by shear localization, while in β-Vit it was due to debonding of the β-phase boundary from the matrix. The spall strengths, at a stain rate of $2\times10^6\ s^{-1}$, were determined to be 2.35 and 2.11 GPa for Vit-1 and β-Vit, respectively. Turneaure et al. (2004) conducted plane shock wave experiments up to 13 GPa on a Zr-based bulk amorphous alloy, $Zr_{56.7}Cu_{15.3}Ni_{12.5}Nb_{5.0}Al_{10.0}Y_{0.5}$, with a quasi-static strength of 2.6 GPa. From the measured particle–velocity histories, the Hugoniot elastic limit (HEL) was determined to be ~7.1 GPa, with a corresponding elastic strain of approximately 4%. For the experiments in which the peak stress exceeded the HEL, a clear two-wave structure consisting of an elastic precursor followed by a plastic wave was observed. Yang et al. (2005) employed a two-stage light gas-gun to investigate the effects of planar shock compression on void formation and crack formation in a Zr-based BMG, $Zr_{41}Ti_{14}Ni_{10}Cu_{12.5}Be_{22.5}$ under hypervelocity impact conditions. More recently, Yang et al. (2006) investigated the damage features in $Zr_{41}Ti_{14}Ni_{10}Cu_{12.5}Be_{22.5}$, subjected to hypervelocity impact using a two-stage light gas-gun. Using scanning electron microscopy they showed that both radial and symmetric cracks were formed on the shocked surface of the target plate when impacted by an aluminum flyer with an impact velocity of 2.7 km/s. Shear bands/cracks parallel to each other, on the cross section close to the shocked surface of the target, were also observed. Mashimo et al. (2006) extended the investigation of BMG under planar shock compression to pressures up to 50 GPa. Using a powder gun and an inclined-mirror photographic technique they investigated the yield behavior and any pressure-induced phase-change in a Zr-based BMG, $Zr_{55}Al_{10}Ni_5Cu_{30}$, while obtaining an HEL of 6.2 GPa. Moreover, a kink was observed in the shock velocity versus particle–velocity relationship (Hugoniot) at about 14 GPa, suggesting the occurrence of a probable shock-induced phase transition. Martin et al. (2007) extended the investigation of BMG under planar shock compression to even higher pressures of up to 123 GPa. Using single-stage and two-stage gas-guns, they investigated the yield behavior and Hugoniot equation of state in a Zr-based BMG, $Zr_{57}Nb_5Cu_{15.4}Ni_{12.6}Al_{10}$. The HEL of the BMG was determined to be 6.86 GPa. The equation of state data showed evidence of a low pressure phase, a transition to a mixed phase region at ~26 GPa, followed by transition to a high pressure phase at ~67 GPa. Yuan et al. (2007a) conducted plate-impact experiments to investigate the shock response of a Zr-based bulk metallic glass, $Zr_{41.25}Ti_{13.75}Ni_{10}Cu_{12.5}Be_{22.5}$, in the normal stress range of 5–7 GPa. The HEL of the BMG was estimated to be 6.15 GPa. Experiments performed at a peak stress exceeding the HEL, yielded a two-wave structure consisting of an elastic precursor followed by a steeply rising plastic wave.

In the present study, an 82.5 mm bore single-stage gas-gun was utilized to obtain spall strength in a zirconium-based BMG, $Zr_{41.25}Ti_{13.75}Ni_{10}Cu_{12.5}Be_{22.5}$, subjected to normal shock compression and combined compression-and-shear loading. A Ti6Al4V flyer plate was used to shock the BMG target plate; the flyer thickness in each experiment was carefully designed so as to produce a state of tension near the center of the BMG target. The particle–velocity profiles were measured at the back (free) surface of the target plate by using the VALYN™ VISAR. In the normal shock-induced compression spall experiments the impact velocities were chosen so as to span the elastic to the elastic–plastic range of the Zr-based BMG during impact, and obtain its spall threshold following controlled levels of normal shock-induced inelasticity in the material. In order to study the effect of shear strain on the spall strength, the normal shock-induced compression in the BMG was kept approximately constant at 5 GPa (i.e. below HEL)

Please cite this article in press as: Yuan, F. , et al. Spall strength of a zirconium-based bulk metallic glass under ... Int. J. Mech. Mater. (2009), doi:10.1016/j.mechmat.2009.01.025

and the skew angle of the projectile was varied from 0° to 24° to vary the shear strain from 0% to 3.18%.

2. Experimental procedure

The material used in the present study was LM-1, supplied by Liquidmetal, Inc., Lake Forest, CA, in the form of rectangular plates with dimensions 90 × 63 × 5 mm. The plates were determined to be fully amorphous by differential scanning calorimetry and X-ray diffraction (Lowhaphandu and Lewandowski, 1998). The as-received plate was then electrical discharge machined (EDM) into smaller circular disks with a diameter of 25.4 mm and thickness of 4.5 mm. The disks were then carefully lapped and polished to a surface finish of 5 μm and used as target plates in the plate-impact experiments as described in Section 2.1.

2.1. Experimental configuration of spall experiments

The plate-impact experiments were conducted using the 82.5 mm bore single-stage gas-gun facility in the Department of Mechanical and Aerospace Engineering at Case Western Reserve University. Fig. 1 shows the schematic of the experimental configuration used for the normal and the combined compression-and-shear plate-impact spall experiments. In the case of the combined compression-and-shear plate-impact experiments the skew angle of the flyer plate was varied from 6° to 24°. The fiberglass projectile (carrying the Ti-6Al-4V flyer plate) was accelerated down the gun barrel by means of compressed air. The rear end of the projectile has a sealing O-ring and a Teflon key that slides in a key-way inside the gun barrel to prevent rotation of the projectile. In order to reduce the possibility of an air cushion between the flyer and target plates impact takes place in a target chamber that has been evacuated to 50 μm of Hg prior to impact. To ensure the generation of plane waves with wave-front sufficiently parallel to the impact face, the flyer and the target plates were carefully aligned to be parallel to within 2×10^{-5} radians by using an optical alignment scheme developed by Kim et al. (1977). The actual tilt between the two plates was measured by recording the times at which four, isolated, voltage-biased pins, that are flush with the surface of the target plate, are shorted to ground. A laser-based optical system utilizing a UNIPHASE Helium-Neon 5 mW laser (Model 1125p) and a high frequency photo-diode, was used to measure the velocity of the projectile within a error of 4%. The multi-beam VALYN VISAR™ (Barker and Hollenbach, 1972) was used to measure the history of the normal particle–velocity at the rear surface of the target plate within a error of 2%. A COHERENT VERDI 5 W solid-state diode-pumped frequency doubled Nd:YVO_4 CW laser with wavelength of 532 nm was used to provide a coherent monochromatic light source. Other details regarding the design, execution and data analysis of the experiments can be found elsewhere (Prakash, 1995).

2.2. Wave propagation in the flyer and the target plates: t–X (time versus distance) and S–V (stress versus particle–velocity) diagrams for the combined compression-and-shear plate-Impact spall experiments

A schematic of the t–X (time vs. distance) diagram, which illustrates the propagation of compression, tensile and shear waves in the target and flyer plates during a typical combined compression-and-shear plate-impact spall experiment, is shown in Fig. 2. The abscissa represents the distance in the target and the flyer plates from the impact surface, while the ordinate represents the time after impact. Upon impact, longitudinal compressive and shear stress waves are generated in both the target and the flyer plates. The solid line represents the longitudinal wave, while the dashed-line represents the shear wave. The arrows indicate the direction of wave propagation. The interaction of the longitudinal release waves from the free-surface of flyer and the target plates results in a tensile state of stress at a pre-determined location within the BMG specimen. If the tensile stress exceeds the critical spall strength for the material, a tensile damage process is initiated and eventually material separation occurs if both the amplitude and the pulse duration of the tensile wave are sufficient. The occurrence of spall can be inferred from the measured free-surface particle–velocity history using the VALYN™ VISAR.

The S–V (stress vs. particle–velocity) diagram details the locus of all the normal stress and particle–velocity

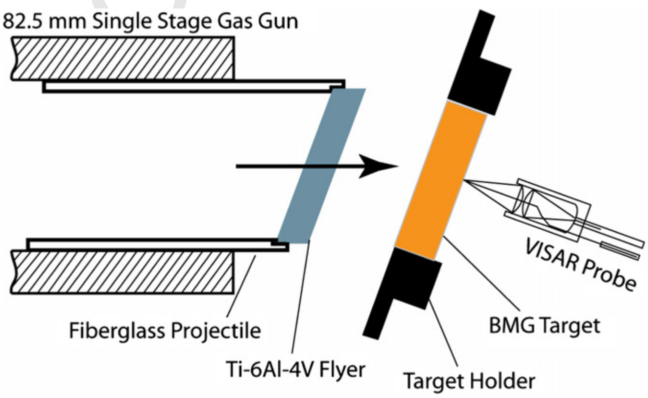

Fig. 1. Schematic of the combined pressure-shear plate-impact spall experiments.

Please cite this article in press as: Yuan, F. , et al. Spall strength of a zirconium-based bulk metallic glass under ... Int. J. Mech. Mater. (2009), doi:10.1016/j.mechmat.2009.01.025

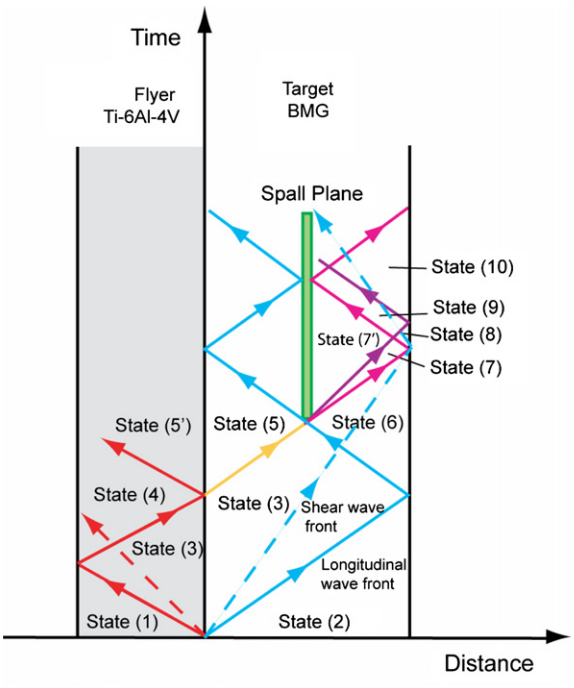

Fig. 2. Wave Propagation in the flyer and the target plates (t–X diagram) for a typical combined compression-and-shear plate-impact spall experiment.

states that can be attained during a typical plate-impact spall experiment. Fig. 3 illustrates the normal stress and particle–velocity in the various shock states. The abscissa represents the particle–velocity while the ordinate represents the normal stress in the target and flyer plates. For the case in which the spall strength is greater than the applied tensile stress, the normal stress and particle–velocity states in the BMG move along the dashed-lines from State (5) to the no-spall-state, denoted by State (7). However, if the tensile stress is greater than the spall strength (σ_{spall} indicated by the short dashed-lines), spallation occurs and the tensile stress in State (7) unloads to the stress-free state denoted by State (7′). The compressive "end of spall" wave from State (7′) arrives at the free-surface of the BMG, and brings the free-surface particle–velocity to State (10), which is the same as that in States (6) and (7′). The free-surface particle–velocity in States (6), (7′), and (10) are referred to as V_{max}, and the corresponding free-surface particle–velocity in State (8) is denoted by V_{min}. The spall strength σ_{spall}, can then be calculated from the measured free-surface particle velocities V_{max} and V_{min} using (Grady and Kipp, 1993),

$$\sigma_{spall} = Z_{BMG}(V_{max} - V_{min})/2. \quad (1)$$

In Eq. (1), Z_{BMG} represents the longitudinal acoustic impedance of the BMG in the zero stress condition.

3. Experimental results and discussions

In the present study, four normal shock-compression spall experiments and six combined compression-and-shear spall experiments were conducted on the Zr-based BMG, $Zr_{41.25}Ti_{13.75}Ni_{10}Cu_{12.5}Be_{22.5}$. The four normal shock-compression spall experiments are designated as FY06011, FY06012, FY06013 and FY06014. Table 1 lists the key parameters for the four experiments – it provides the Shot #, thickness of the BMG target plate, thickness of the Ti-6Al-4V flyer plate, impact velocity, and the shock-induced compressive stress. The shock-induced compressive stresses were estimated from the measured impact velocity, the knowledge of the elastic longitudinal impedance of the BMG, and the shock Hugoniot of the Ti-6Al-4V flyer plate (Meyers, 1994). The details of these calculations are provided in Section 3.2. The dimensions of the flyer and target plates were chosen so as to avoid the arrival of the release waves from the lateral boundary at the monitoring point of the target plate during the time duration of interest. The impact velocities were chosen so as to span the elastic to the elastic–plastic range of the Zr-based BMG material. The BMG is expected to remain elastic at impact velocities of 328.9 and 383.8 m/s (which correspond to impact stresses of 4.39 and 5.13 GPa, respectively), but show significant inelasticity at the higher impact velocities of 463.7 and 541.8 m/s (which correspond to impact stresses of 6.06 and 7.06 GPa, respectively).

The six combined compression-and-shear spall experiments are designated as FY06011, FY06015, FY06016, FY06017, FY06018, FY06019 and FY06020. Table 2 lists the key parameters for the six experiments – it provides

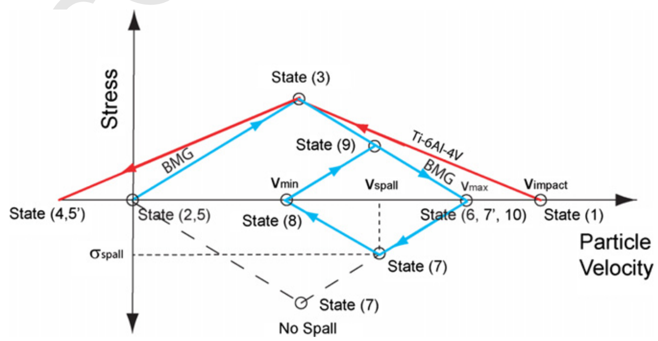

Fig. 3. Normal stress versus particle–velocity (S–V) diagram for a typical normal plate-impact spall experiment. The dashed-line shows the hypothetical case for the no-spall condition.

Table 1
Summary of the normal spall experiments on the Zr-based bulk metallic glass, $Zr_{41.25}Ti_{13.75}Ni_{10}Cu_{12.5}Be_{22.5}$.

Exp. No.	Flyer Ti-6Al-4V (mm)	Target BMG (mm)	Impact velocity (m/s)	Impact stress (GPa)
FY06014	3.1	4.3	328.9	4.39
FY06011	3.1	4.6	383.8	5.13
FY06012	3.1	4.1	463.7	6.06
FY06013	3.1	4.2	541.8	7.06

Table 2
Summary of the pressure-shear spall experiments on the Zr-based bulk metallic glass, $Zr_{41.25}Ti_{13.75}Ni_{10}Cu_{12.5}Be_{22.5}$.

Exp. No.	Flyer Ti-6Al-4V (mm)	Target BMG (mm)	Impact velocity (m/s)	Skew angle (°)	Impact stress (GPa)	Shear strain (%)
FY06020	3.1	4.4	411.8	6	5.44	0.90
FY06015	3.1	4.2	399.7	12	5.06	1.66
FY06019	3.1	4.5	383.9	15	4.87	2.03
FY06018	3.1	4.5	389.1	18	4.81	2.40
FY06016	3.1	3.9	404.8	20	4.95	2.76
FY06017	3.1	3.9	391.1	24	4.83	3.18

the Shot #, thickness of the BMG target plate, thickness of the Ti-6Al-4V flyer plate, impact velocity, skew angle, the shock-induced normal stress and shear strain. The shock-induced compressive stresses were estimated from the measured impact velocity, the skew angle, the knowledge of the elastic longitudinal impedance of the BMG and the shock Hugoniot for the Ti-6Al-4V flyer plate. The shear strains were estimated from the measured impact velocity, the skew angle and the shear impedances of the BMG target and the Ti-6Al-4V flyer plates. In the combined compression-and-shear experiments the normal impact stress in the six experiments was kept approximately constant at ~5 GPa (i.e. below HEL of the BMG). The skew angle is varied from 0° to 24° – the corresponding shear strain varies from 0% to 3.18%. Table 3 lists the physical properties of the BMG, $Zr_{41.25}Ti_{13.75}Ni_{10}Cu_{12.5}Be_{22.5}$, used in the present plate-impact experiments.

3.1. Calculation of spall strength in the Zr-based BMG

Fig. 4 shows the measured free-surface particle–velocity profile and the corresponding *t–X* diagram for a typical normal plate-impact experiment, Shot FY06011. At time T1, the free-surface particle–velocity increases to a level of V_{max} at the arrival of the longitudinal compression wave at the free-surface of the BMG target plate. At time T2, the release waves from the back surfaces of the target and the flyer plates intersect at a pre-determined location within the BMG target plate; the corresponding "unloading tensile wave" and the "end of spall compressive wave" propagate and arrive at the free-surface of the BMG plate at times T3 and T4, respectively. Upon arrival of the unloading tensile wave (at time T3) the particle–velocity at the free-surface of the BMG plate starts to decrease, and at time T4 reaches a level of V_{min}. This decrease in the particle–velocity is followed by recovery in particle–velocity to its Hugoniot state of V_{max}, which is also referred to as the "pull-back" characteristic of the spall signal; the magnitude of the pull-back signal is used in the calculation of the material's spall strength using Eq. (1). Since the first Hugoniot state is not at a constant level, V_{max} was taken to be the average value of the platea, which leads to an error of approximately 2% for the spall strength calculation. For the case in which there is no spall, the free-surface particle–velocity remains at its steady state level of V_{no_spall}. V_{no_spall} corresponds to State (7) in Fig. 3, when the tensile stress is not high enough to create spall.

3.2. Calculation of shock-induced normal stress and shear strain

In the present work, in order to estimate the shock-induced stress at the flyer and the target interface, the Equation of State (EOS) for the flyer and elastic longitudinal impedance of the BMG target material are utilized. For most materials, the EOS can be approximated as a linear relationship between the shock velocity and the particle–velocity (U_s vs. u_p) given by

$$U_s = C_0 + Su_p \tag{2}$$

where, S is a experimentally determined parameter, and C_0 is the sound velocity in the material at zero pressure (Meyers, 1994).

For Ti-6Al-4V, the Equation of State can be written as (Meyers, 1994)

$$U_s = 5.139 + 0.855u_p. \tag{3}$$

Using the Rankine-Hugoniot conservation relationships, the Hugoniot stress σ_H, at the flyer target interface can be determined by the relations

$$\sigma_H = \rho_0^{BMG} C_L^{BMG} u_p \tag{4}$$

$$\sigma_H = -\rho_0^{Ti6Al4V}(C_0^{Ti6Al4V} + S^{Ti6Al4V}u_p)(u_p - u_I\cos(\theta)) \tag{5}$$

In Eqs. (4) and (5), ρ_0^{BMG} and $\rho_0^{Ti6Al4V}$ are initial densities of the BMG and Ti-6Al-4V, respectively; C_L^{BMG} is longitudinal wave speed of the BMG; $C_0^{Ti6Al4V}$ and $S^{Ti6Al4V}$ are constants in the Equation of State for Ti-6Al-4V; u_I is the impact velocity; and θ is the skew angle of impact. Ideally, the calculation of Hugoniot stress should take into account the Hugoniot Elastic Limit (HEL) of Ti-6Al-4V, which varies be-

Table 3
Physical properties of the Zr-based BMG (Vit-1) used in the present investigation, taken from Lu (2002).

Density	Longitudinal wave speed (m/s)	Shear wave speed (m/s)	Bulk wave speed (m/s)	Elastic modulus (GPa)	Shear modulus (GPa)	Bulk modulus (GPa)	Poisson's ratio
6000 kg/m^3	5185	2464	4335	98.6	36.4	113	0.354

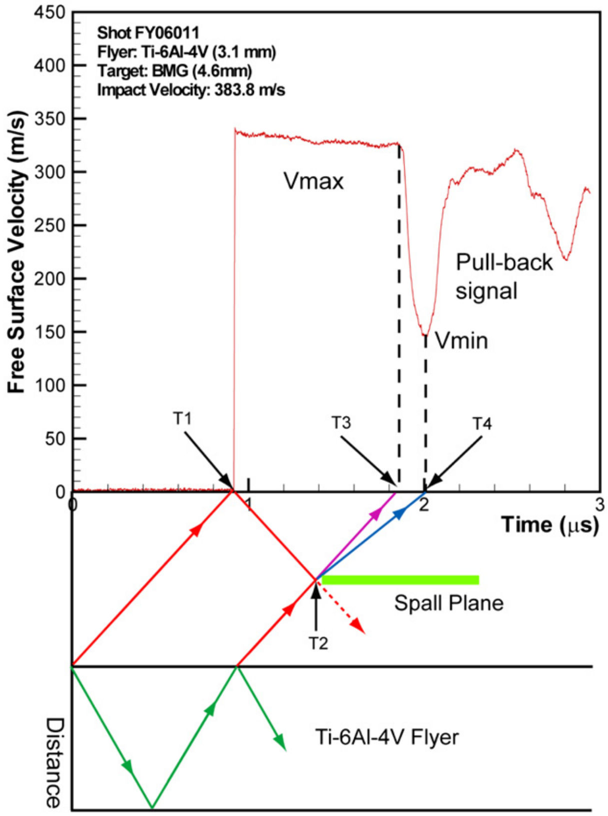

Fig. 4. Time-distance diagram paired with the measured free-surface particle–velocity profile for experiment FY06011 to illustrate the "pull-back" spall signal.

tween 2.0 and 2.8 GPa (Arrieta and Espinosa, 1999). The Hugoniot stresses in the present experiments are above 5 GPa, and the effect of neglecting the HEL of Ti-6Al-4V in the calculation of the Hugoniot stresses in the BMG using Eq. (5) is within the uncertainties of other measurements (i.e. 5%).

The shear strain in the pressure-shear spall experiments can be calculated by using the measured impact velocity, the skew angle of impact, and the shear impedances of the BMG target and the Ti-6Al-4V flyer plates as (Yuan et al., 2007b)

$$\varepsilon_{\text{shear}} = \frac{u_I \sin(\theta)\rho_0^{\text{Ti6Al4V}} C_s^{\text{Ti6Al4V}}}{(\rho_0^{\text{Ti6Al4V}} C_s^{\text{Ti6Al4V}} + \rho_0^{\text{BMG}} C_s^{\text{BMG}}) C_s^{\text{BMG}}}, \tag{6}$$

where C_s^{BMG} and C_s^{Ti6Al4V} are shear wave speed of the BMG and Ti6Al4V plates, respectively.

3.2.1. Spall strength of the Zr-based BMG under normal shock-induced compression

Fig. 5 shows the measured free-surface particle–velocity profiles for the four normal plate-impact spall experiments – FY06014, FY06011, FY06012, and FY06013 – conducted at impact velocities of 328.9, 383.8, 463.7, and 541.8 m/s, respectively. The corresponding shock-induced compressive stresses for the four experiments were 4.39, 5.13, 6.06, and 7.06 GPa. Fig. 6 shows the spall strength data collected from the four normal plate-impact spall experiments conducted in the present study on $Zr_{41.25}Ti_{13.75}Ni_{10}Cu_{12.5}Be_{22.5}$ as well as the two normal plate-impact experiments conducted by Zhuang et al. (2002) on $Zr_{41.2}Ti_{13.8}Ni_{10}Cu_{12.5}Be_{22.5}$ (Vit-1) and its composite $Zr_{56.3}Ti_{13.8}Ni_{5.6}Cu_{6.9}Be_{12.5}$ (β-Vit). The Hugoniot Elastic Limit (HEL) for $Zr_{41.25}Ti_{13.75}Ni_{10}Cu_{12.5}Be_{22.5}$ was estimated to be $\sigma_{\text{HEL}} \sim 6.15$ MPa in the previous work by Yuan et al. (2007a), indicating that Experiments FY06011 and FY06014 were conducted below the HEL stress level, while Experiments FY06012 and FY06013 were conducted above the HEL stress level. It is interesting to note that the spall strength of the Zr-based BMG decreases with increasing levels of shock compression below the HEL; at shock-compression levels above the HEL the spall strength remains essentially constant up to 7.06 GPa, the highest stress level obtained in the present series of experiments.. The measured spall strengths at shock-compression levels of 7.06, 6.06, 5.13 and 4.39 GPa were 2.33, 2.35, 2.72, and 3.5 GPa, respectively. These levels of spall strength are in close agreement to those measured by Zhuang et al. (2002) on Vit-1 and β-Vit in the input stress range of 5–7 GPa, as illustrated in Fig. 6. It must be noted, however, that the stress pulse duration in the experiments conducted by Zhuang et al. was approximately 0.46 μs when compared with approximately 1.1 μs used in the present investigation. Moreover, they did not conduct any spall experiment in the shock-induced stress range <5 GPa.

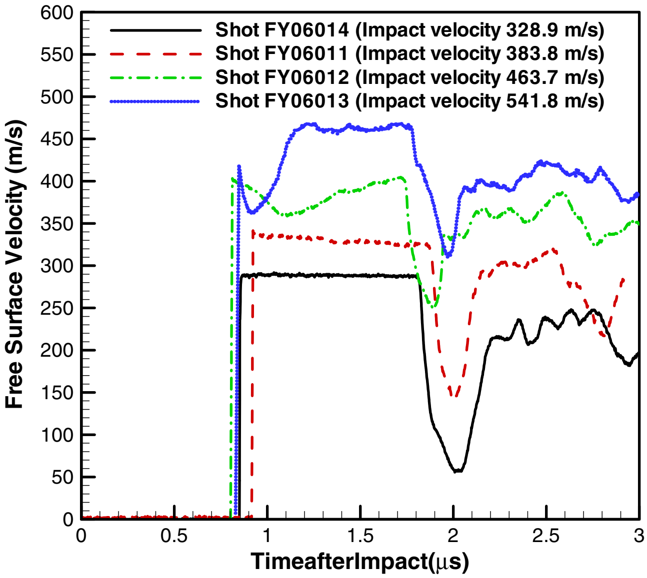

Fig. 5. Free-surface particle–velocity versus time profiles for the four normal plate-impact spall experiments conducted in the present study.

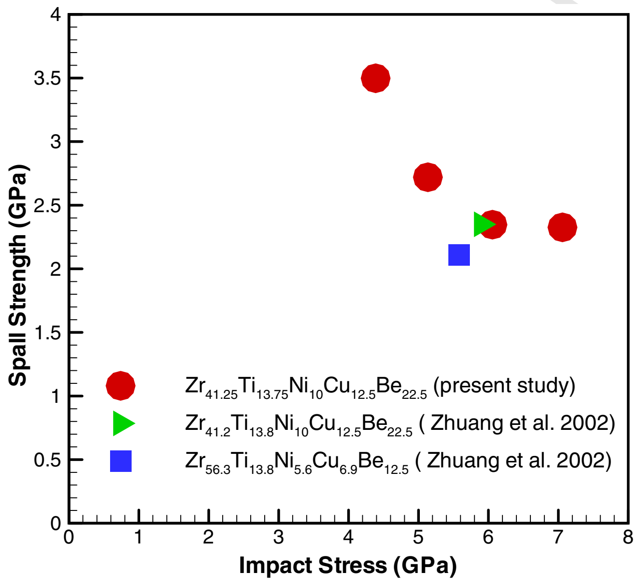

Fig. 6. Spall strength as a function of impact stress for three different Zr-based BMGs (from Yuan, 2007a). It is to be noted that the spall experiments conducted by Zhuang et al. had a pulse width of 0.46 μs.

The decrease in the spall strength with increasing levels of shock compression (below the HEL) is indicative of the accumulation and dominance of brittle deformation (damage) within the BMG due to the shock-induced compression. On the other hand, the observed stabilization of spall strength at shock-compression levels above the HEL are understood to be due to the onset of ductile inelastic processes within the BMG, which counteracts the effects of brittleness due to the accumulation of damage.

Similar variations in spall strength have been reported previously in nominally brittle materials, e.g. sintered and hot pressed silicon carbide (SiC), subjected to planar shock compression (Bartkowski and Dandekar, 1996; Dandekar, 2004). In these studies the spall threshold of the two SiCs were observed to increase as the normal stress was increased from 1.6 to 3.7 GPa; above 3.7 GPa, the spall threshold decreased with an increase in impact stress up to 12 GPa. Both materials appeared to peak in spall threshold at an impact stress of about 3.7 GPa. This unusual trend in the spall strength of the silicon carbides was explained to be due to the competing roles of, (i) localized plasticity, and (ii) generation and propagation of cracks taking into consideration their relative dominance below and above a given magnitude of stress. The initial increase in spall strength, with an increase in shock-induced stress, was likely due to the dominance of localized plastic deformation over crack-dominated brittle deformation, while the corresponding decline in spall strength with an increase in shock-induced stress is attributed to the dominance of crack-induced brittle deformation over plastic deformation. Moreover, similar mechanical behavior was also observed by Nathenson et al. (2005) on ASA-800 Si_3N_4, where the spall strength was observed to decrease with an increase in the shock-induced normal stress. The spall strength at stress levels below the HEL were found to decrease by almost 37% from its maximum measured value of 0.9 GPa as the impact velocity was increased from 65 to 599 m/s. Moreover, as also observed for the BMG in the present investigation, the rate of drop in spall strength with an increase in shock-induced stress is observed to be relatively high in the beginning and then levels off as the stress levels approach the HEL for the material.

3.3. Spall strength of the Zr-based BMG under combined compression-and-shear: effect of shear strain

Fig. 7 shows the measured free-surface normal particle–velocity profiles for the six pressure-shear spall experiments (FY06020, FY06015, FY06019, FY06018, FY06016 and FY06017) conducted at the impact velocities of 411.8, 399.7, 383.9, 389.1, 404.8 and 391.1 m/s, respectively. The skew angles for these seven experiments were 6°, 12°, 15°, 18°, 20° and 24°, respectively. The corresponding shock-induced stresses for the seven experiments were 5.44, 5.06, 4.87, 4.81, 4.95 and 4.83 GPa. Since these experiments were conducted at similar normal impact stress levels but different shear strains, the results can be used to evaluate the effect of shear strain on the spall strength of the Zr-based BMG. It is interesting to note that for experiments FY06018 and FY0619, the free-surface particle–velocity profiles unload completely to their no-spall levels (i.e. zero particle–velocity), and are followed by a pull-back signal, indicating that the spall strengths are nearly equal to the applied tensile stress of 4.75 GPa.

Fig. 8 shows the spall strength vs. shear strain data collected from one normal impact spall experiment (FY06011) and the six pressure-shear spall experiments. With increasing levels of shear strain the spall strength of the BMG was found to initially decrease slightly till about 2% shear strain; increase dramatically to 4.75 GPa at shear strains in the range of 2–2.4%; and then fall steeply as the shear strain is increased from 2.4% to 3.2%. This observed trend in spall strength as a function of increasing shear strain is much different from that previously observed in other engineering materials. For example, in the work of Nathenson (2005) on ASA-800 Si_3N_4, the presence of shear strain following normal shock compression resulted in a severe degradation of the spall strength. In particular, the spall strength was reduced to essentially zero at a normal stress of 6.93 GPa at a shear strain of approximately 0.4%. Besides Si_3N_4, spall strength was also found to decrease with increasing shear strain in S2-glass and E-glass fiber-reinforced polymer composites in Yuan's work (2007b).

This unusual trend in the shear strain on the spall strength of the Zr-based BMG can perhaps be explained by the competing roles of localized ductile inelasticity and brittle damage, taking into consideration their relative dominance below and above a given magnitude of shear strain. The sudden increase in spall strength of the BMG at around 2% shear strain (FY06019 and FY06018), is likely due to the prevalence of shear-induced inelasticity over shear-crack dominated localized brittle deformation during the combined compression-and-shear loading, while the decline in spall threshold with a further increase in shear strain (FY06016 and FY06017) can be attributed to the re-establishment of the shear-crack dominated mode of brittle deformation.

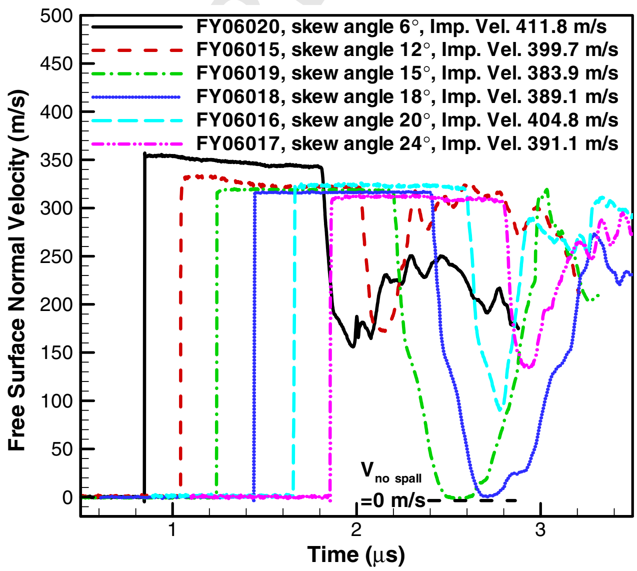

Fig. 7. Free-surface normal particle–velocity versus time profiles for the six combined compression-and-shear spall experiments conducted in the present study. The free-surface particle–velocity curves have been shifted to the right to avoid overlapping curves of similar shapes and sizes.

Please cite this article in press as: Yuan, F. , et al. Spall strength of a zirconium-based bulk metallic glass under ... Int. J. Mech. Mater. (2009), doi:10.1016/j.mechmat.2009.01.025

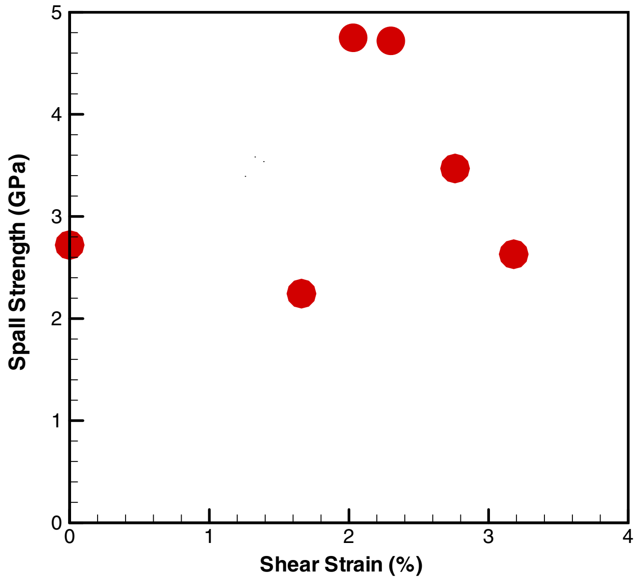

Fig. 8. Spall strength as a function of shear strain for one normal impact spall experiment and six combined compression-and-shear spall experiments conducted in the present study. The normal component of the impact stress is maintained at ∼5 GPa in all the seven experiments.

3.4. Scanning electron microscopy of the spall/fracture surfaces

In order to better understand the state of damage in the BMG specimen following normal shock-induced compression and combined compression-and-shear loading, scanning electron microscopy (SEM) was used to examine the spall surface morphology following tensile spall in the post-test recovered fragments.

Bulk metallic glasses are, at best, quasi-brittle materials, because they do not possess sufficient intrinsic micro-mechanisms to mitigate high stress concentrations at crack tips. Contributing to this are an absence of strain hardening, and a lack of intrinsic crack propagation barriers such as grain boundaries. The fracture surface morphology exhibits a characteristic "vein" or "river" pattern. In contrast, brittle fracture is reflected as a relatively smooth fracture morphology. However, higher magnification imaging shows that even the smooth fracture surfaces also have a vein morphology, albeit on a much finer scale. During unstable fracture the material is fluid-like, and the scale of the vein pattern has been estimated by applying Taylor's meniscus instability criterion to determine the critical wavelength of the instability (Argon and Salama, 1976). Therefore, the scale of the vein pattern on the fracture surface should, in principle, be indicative of the toughness of a given metallic glass. Indeed, recent experimental results show that the fracture morphology of "tough" glasses are rough with a deep vein morphology whereas the brittle glasses have very shallow (nanometer scale) vein patterns.

Two normal plate-impact spall experiments, i.e. FY06012 and FY06014, were chosen for the post-test microstructural analysis. Experiment FY06014 was conducted at a normal stress level below the HEL, while experiment FY0612 was conducted at a shock-compression level above the HEL. Fig. 9 shows the high magnification SEM pictures of the failure morphology at the spall plane for the two experiments. The failure surfaces reveal extensive veining, indicating that local failure occured by a local drop in material viscosity during the material separation (spall) process. It is interesting to note that the spall surfaces are flat with relatively with low density veining with fine features at impact stress levels below the HEL, suggesting that perhaps the density of shear-induced brittle failure dominates the material separation process during spall in this case. However, the observed veining is much *coarser* and more dense when the shock-compression level is above the HEL, as seen from the higher magnification SEM image of the spall plane in Fig. 9b, indicating the dominance of local shear-induced inelastic flow of low viscosity material during spall. In view of these observations, the decrease in the spall strength with increasing levels of normal stress below the HEL can be attributed to the dominance of shear-crack induced brittle damage within the BMG as the impact stresses are increased. However, the rate spall strength levels off at shock-induced compression stress levels above the HEL due to accumulation of relatively low viscosity local inelastic flow during material separation in the BMG.

In order to understand the effects of the combined compression-and-shear loading on the spall strength of the BMG, SEM fractographs of the spall surface from the four combined compression-and-shear experiments, i.e. FY06015, FY06018, FY06016 and FY06017, were examined. The four experiments were conducted at a normal impact stress of approximately 5 GPa (below the HEL). The skew angles used in these experiments were 12°, 18°, 20° and 24°, respectively. The corresponding shear strains were 1.66%, 2.40%, 2.76% and 3.18%, respectively. Fig. 10 shows the SEM fractograph of the spall surfaces from the four experiments. From these micrographs it can be seen that for the case of the combined compression-and-shear load-

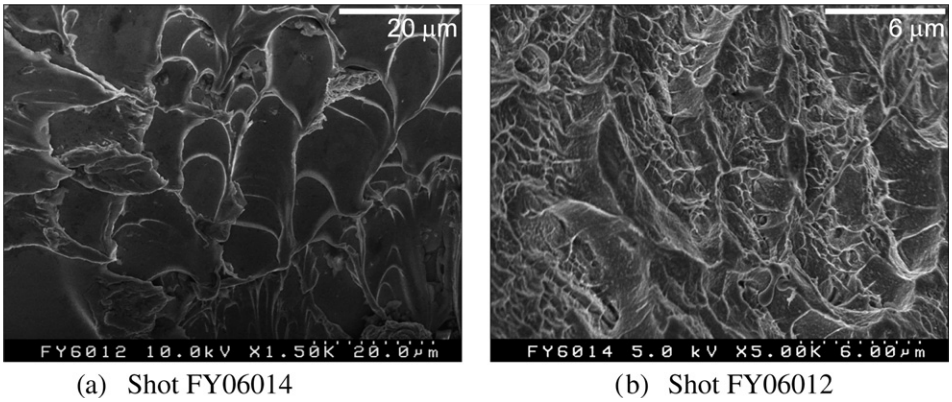

Fig. 9. Scanning electron microscope pictures of spall surfaces for two normal plate-impact spall experiments. (a) With normal component of the impact stress below the HEL; (b) with the normal stress above HEL.

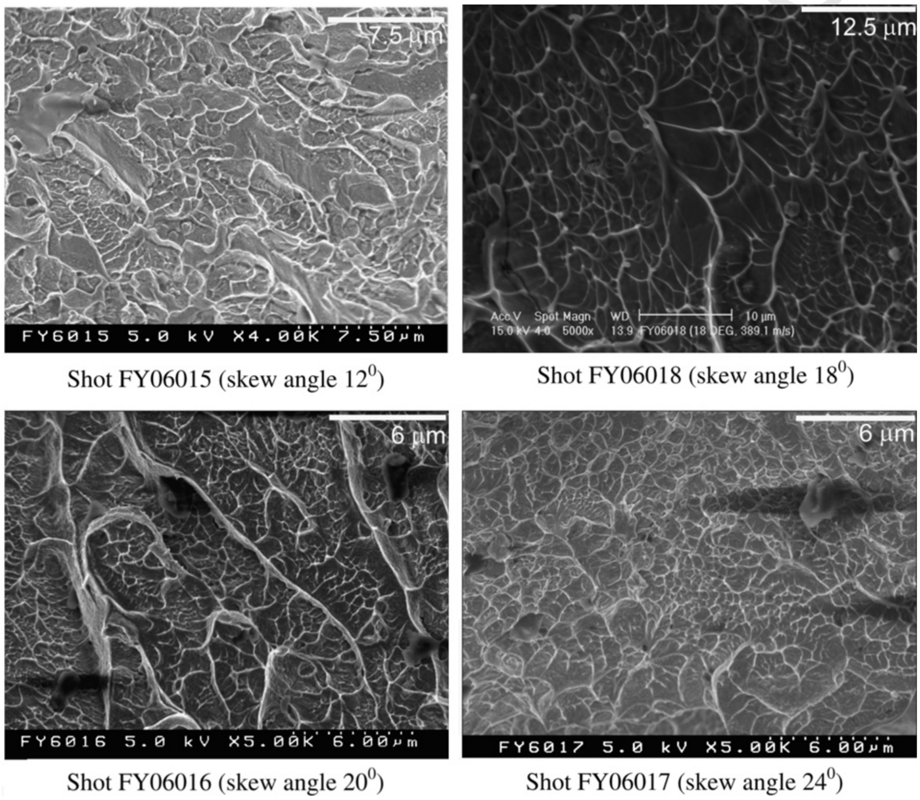

Fig. 10. Scanning electron microscope pictures of spall/fracture surfaces for four pressure-shear plate-impact spall experiments.

ing, even when the compression stress is below the HEL, a much higher density and coarser vein features (when compared to that observed for experiment FY06012, i.e. normal spall test with normal stress level below the HEL) are obtained. Besides the higher density of veining, experiments FY06016 and FY06018 also show coarser vein structures (higher roughness) in the SEM micrographs when compared to the other combined compression-and–shear spall experiments. These coarser vein structures are indicative of higher levels of inelastic flow of low viscosity material in the BMG samples for these two experiments, and could provide a plausible reason for the observed increase in spall strength of the BMG.

4. Summary

In the present study a series of plate-impact experiments was conducted to study the spall strength of the Zr-based BMG under normal shock-compression and combined compression-and-shear loading. The BMG samples were shock loaded by utilizing Ti-6Al-4V flyer plates up to ~7 GPa. For the combined compression-and-shear plate-impact experiments, skew angles in the range of 6–24° were employed. From the results of the normal plate-impact spall experiments, the spall strength of BMG was found to decrease with increasing levels of impact stress below the HEL. However, the rate of drop in spall strength levels off as the shock-induced compression stresses approach the HEL. The spall strength at a normal stress of 4.4 GPa was 3.5 GPa, while the spall strengths at normal stresses of 5.1, 6.0 and 7.0 GPa were 2.72, 2.35 and 2.33 GPa, respectively. In the case of the combined compression-and-shear experiments, the spall strength of the BMG was found to decrease initially with increasing shear strain, and then increases dramatically to 4.75 GPa at ~2% shear strain, followed by a more significant decrease as the shear strain was increased from 2.40% to 3.18%. This unusual trend in the effects of shear strain on the spall strength of the Zr-based BMG can perhaps be explained by the competing roles of localized inelastic flow of low viscosity BMG material and accumulation of shear-crack induced damage taking into consideration their relative dominance below and above a critical shear strain.

Acknowledgments

The authors acknowledge Case Western Reserve University (Case Graduate Student Prime Fellowship program) and the Office of Naval Research (ONR-N00014-03-1-0205) for providing the bulk of financial support for conducting the present research. Recent additional support was provided by ONR-N00014-07-1. The authors also acknowledge the Major Research Instrumentation awards MRI CMS 0079458 and MRI CMMI 0521364 by the National Science Foundation for the acquisition of the multi-beam VALYN VISAR and the high resolution SEM used in the present experiments.

References

Argon, A.S., Salama, M., 1976. The mechanism of fracture in glassy materials capable of some inelastic deformation. Materials Science & Engineering A 23, 219–230.

Arrieta, H.V., Espinosa, H.D., 1999. High and low temperature dynamic testing of advanced materials. In: Furnish, M.D., Chhabildas, L.C., Hixson, R.S. (Eds.), Shock Compression of Condensed Matter-1999. American Institute of Physics, New York, pp. 1075–1078.

Bach, J., Krueger, B., Fultz, B., 1991. Shock wave consolidation of a Ni-Cr-Si-B metallic-glass powder. Materials Letters 11, 383–388.

Barker, L.M., Hollenbach, R.E., 1972. Laser interferometer for measuring high velocities of any reflecting surface. Journal Applied Physics 43, 4669–4675.

Bartkowski, P.T., Dandekar, D.P., 1996. Spall strengths of sintered and hot pressed silicon carbide. In: Schmidt, S.C., Tao, W.C. (Eds.), Shock Compression of Condensed Matter-1995. American Institute of Physics, New York, pp. 535–539.

Bruck, H.A., 1994. Quasi-static and Dynamic Constitutive Characterization of Beryllium-bearing Bulk Metallic Glasses. California Institute of Technology, Pasadena, CA.

Bruck, H.A., Rosakis, A.J., Johnson, W.L., 1996. The dynamic compressive behavior of beryllium bearing bulk metallic glasses. Journal of Materials Research 11, 503–511.

Conner, R.D., Dandliker, R.B., Scruggs, V., Johnson, W.L., 2000. Dynamic deformation behavior of tungsten-fiber/metallic-glass matrix composites. International Journal of Impact Engineering 24, 435–444.

Dandekar, D.P., 2004. Spall strength of silicon carbide under normal and simultaneous compression-shear shock wave loading. International Journal of Applied Ceramic Technology 1, 261–268.

Grady, D.E., Kipp, M.E., 1993. Dynamic fracture and fragmentation. In: Asay, J.R., Shahinpoor, M. (Eds.), High-Pressure Shock Compression of Solids. Springer-Verlag, New York, pp. 265–322.

Hays, C.C., Kim, C.P., Johnson, W.L., 2000. Enhanced plasticity of bulk metallic glasses containing ductile phase dendrite dispersions, International Symposium on Metastable, Mechanically Alloyed and Nanocrystalline Materials (ISMANAM 99). Dresden, Germany. pp. 191–196.

Hufnagel, T.C., Jiao, T., Li, Y., Xing, L.Q., Ramesh, K.T., 2002. Deformation and failure of $Zr_{57}Ti_5Cu_{20}Ni_8Al_{10}$ bulk metallic glass under quasi-static and dynamic compression. Journal of Materials Research 17, 1441–1445.

Johnson, W.L., 1999. Bulk metallic glasses. In: Johnson, W.L., Inoue, A., Liu, C.T. (Eds.), MRS Symposium Proceedings. Materials Research Society, pp. 311–339.

Kim, K.S., Clifton, R.J., Kumar, P., 1977. A combined normal and transverse displacement interferometer with an application to impact of Y-cut Quartz. Journal of Applied Physics 48, 4132–4139.

Lowhaphandu, P., Lewandowski, J.J., 1998. Fracture toughness and notched toughness of bulk amorphous alloy: Zr-Ti-Ni-Cu-Be. Scripta Materialia 38, 1811–1817.

Lu, J., 2002. Mechanical Behavior of a Bulk Metallic Glass and its Composites Over a Wide Range of Strain Rates and Temperatures. California Institute of Technology, Pasadena, CA.

Martin, M., Sekine, T., Kobayashi, T., Kecskes, L., Thadhani, N.N., 2007. High-pressure equation of the state of a zirconium-based bulk metallic glass. Metallurgical and Materials Transactions A 8, 1–2. doi: 10.1007/s11661-007-9263-x.

Mashimo, T., Togo, H., Zhang, Y., Uemura, Y., Kawamura, Y., 2006. Shock-compression behavior of Zr-based metallic glass. In: Khan, A.S., Kazmi, R. (Eds.), 12th International Symposium on Plasticity and its Applications. Anisotropy, Texture, Dislocations and Multiscale Modeling in Finite Plasticity and Viscoplasticity and Metal Forming. Neat, Inc., Fulton, MD., Halifax, Nova Scotia, Canada, pp. 157–159.

Meyers, M.A., 1994. Dynamic Behavior of Materials. John Wiley & Sons, New York, NY.

Nathenson, D.I., Prakash, V., Dandekar, D.P., 2005. Dynamic response of silicon nitride under combined pressure and shear impact, Paper # 315 (s22). In: Proceedings of the 2005 SEM Annual Conference and Exposition on Experimental and Applied Mechanics. Society of Experimental Mechanics, Bethel, Connecticut, USA, Portland, Oregon, USA.

Prakash, V., 1995. A pressure-shear plate impact experiment for investigating transient friction. Experimental Mechanics 35, 329–336.

Subhash, G., Zhang, H., Li, H., 2003. Thermodynamic and Mechanical behavior of hafnium/zirconium based bulk metallic glasses. In: Bodner, S.R., Rittel, D., DSherman, D. (Eds.), Proceedings of the International Conference of Mechanical Behavior of Materials (ICM-9). Kenes International, Geneva, Switzerland, p. 1A5.

Sunny, G.P., Prakash, V., Lewandowski, J.J., 2005a. Effects of annealing on dynamic behavior of a bulk metallic glass, Paper # IMECE2005-83016. In: Proceedings of the 2005 International Mechanical Engineering Conference and Exposition, ASME. American Society of Mechanical Engineers, New York, NY, Orlando, FL.

Sunny, G.P., Yuan, F., Lewandowski, J.J., Prakash, V., 2005b. Dynamic Stress–Strain response of $Zr_{41.25}$ $Ti_{13.75}$ Ni_{10} $Cu_{12.5}$ $Be_{22.5}$ based bulk metallic glass, Paper # 324. In. Proceedings of the 2005 SEM Annual Conference and Exposition on Experimental and Applied Mechanics. Society of Experimental Mechanics, Portland, Oregon USA.

Sunny, G.P., Lewandowski, J.J., Prakash, V., 2006a. Dynamic compression of amorphous and annealed bulk metallic glass, Paper # 349. In: Proceedings of the 2006 SEM Annual Conference and Exposition on Experimental and Applied Mechanics. Society of Experimental Mechanics, St. Louis, MO, USA.

Sunny, G.P., Prakash, V., Lewandowski, J.J., 2006b. Results from a novel insert design for high starin-rate compression of a bulk metallic glass, Paper # IMECE2006-15414. In: Proceedings of the 2006 International Mechanical Engineering Conference and Exposition, ASME. American Society of Mechanical Engineers, New York, NY, Chicago, IL.

Turneaure, S.J., Winey, J.M., Gupta, Y.M., 2004. Compressive shock wave response of a Zr-based bulk amorphous alloy. Applied Physics Letters 84, 1692–1694.

Yang, C., Liu, R.P., Zhang, B.Q., Wang, Q., Zhan, Z.J., Sun, L.L., Zhang, J., Gong, Z.Z., 2005. Void formation and cracking of $Zr_{41}Ti_{14}Cu_{12.5}$–$Ni_{10}Be_{22.5}$ bulk metallic glass under planar shock compression. Journal of Materials Science 40, 3917–3920.

Yang, C., Wang, W.K., Liu, R.P., Zhang, X.Y., Li, X., 2006. Damage features of $Zr_{41}Ti_{14}Cu_{12.5}Ni_{10}$Be22.5 bulk metallic glass impacted by hypervelocity projectiles. Journal of Spacecraft and Rockets 43, 565–567.

Yuan, F., Prakash, V., Lewandowski, J.J., 2007a. Spall strength and Hugoniot elastic limit of a Zirconium-based bulk metallic glass under planar shock compression. Journal of Materials Research 22, 402–411.

Yuan, F., Tsai, L., Prakash, V., Dandekar, D.P., Rajendran, A.M., 2007b. Spall strength of glass-fiber reinforced polymer composites. International Journal of Solids and Structures 44, 7731–7747.

Zhuang, S.M., Lu, J., Ravichandran, G., 2002. Shock wave response of a zirconium-based bulk metallic glass and its composite. Applied Physics Letters 80, 4522–4524.